Catalysis Science & Technology

Validation of the Cossee-Arlman Mechanism for Propylene Oligomerization on Ni/UiO-66

Journal:	*Catalysis Science & Technology*
Manuscript ID	CY-ART-04-2023-000570.R1
Article Type:	Paper
Date Submitted by the Author:	13-Jun-2023

Complete List of Authors:	Yeh, Benjamin; University of Minnesota, Chemical Engineering and Materials Science Chheda, Saumil; University of Minnesota, Chemical Engineering and Materials Science; University of Minnesota, Department of Chemistry, Chemical Theory Center, and Supercomputing Institute Zheng, Jian; Pacific Northwest National Laboratory Schmid, Julian; Pacific Northwest National Laboratory, Catalysis Science Löbbert, Laura; Technische Universität München, Lehrstuhl für Technische Chemie II Bermejo-Deval, Ricardo; Technische Universität München, Lehrstuhl für Technische Chemie II Gutiérrez Tinoco, Oliver; Pacific Northwest National Laboratory, Catalysis Science Lercher, Johannes; Technische Universität München, Lehrstuhl für Technische Chemie II; Pacific Northwest National Laboratory, Catalysis Science Gagliardi, Laura; University of Chicago Department of Chemistry, Bhan, Aditya; University of Minnesota, Chemical Engineering and Materials Science

ARTICLE

Validation of the Cossee-Arlman Mechanism for Propylene Oligomerization on Ni/UiO-66

Received 00th January 20xx,
Accepted 00th January 20xx

DOI: 10.1039/x0xx00000x

Benjamin Yeh,[a] Saumil Chheda,[a,b] Jian Zheng,[c] Julian Schmid,[c] Laura Löbbert,[d] Ricardo Bermejo-Deval,[d] Oliver Y. Gutiérrez,[c] Johannes A. Lercher,[c,d] Laura Gagliardi,[e] and Aditya Bhan[a,*]

Steady state rates expressions can be derived to distinguish the Cossee-Arlman and metallacycle mechanisms postulated for propylene oligomerization on nickel-based catalysts based on product selectivities, where product selectivities for the former are a function of olefin pressure because sequential coordination and insertion steps lead to independent mechanistic pathways for different hexene isomers. In contrast, the metallacycle mechanism presents pressure-independent product selectivities due to successive coordination prior to the kinetically relevant steps in each mechanism. In this work, steady state propylene oligomerization rates and selectivities were measured in the absence of an activator on nickel functionalized UiO-66 metal organic framework (MOF), Ni/UiO-66, to validate the Cossee-Arlman mechanism for light olefin oligomerization. In-situ NO titrations reveal that ~5% of nickel sites were active during the reaction, and thus, not all nickel sites are relevant for catalysis. Propylene dimerization was first order in propylene pressure from 5 to 500 kPa with an apparent activation energy of ~20 kJ mol^{-1} from 453 to 493 K. Calculated apparent activation energies with density functional theory (DFT) calculations on cluster models of Ni/UiO-66 are in agreement with experiment to corroborate the Cossee-Arlman mechanism. Selectivities of hexene products and the ratio of hexene product selectivities on Ni/UiO-66 are in accordance with selectivity expressions derived from the Cossee-Arlman mechanism. Analysis of product selectivities can be used more extensively to demarcate the Cossee-Arlman and metallacycle mechanisms for olefin oligomerization on metal-based catalysts.

1. Introduction

The Shell Higher Olefin Process (SHOP) that is practiced industrially accomplishes homologation of ethylene to linear alpha olefins (LAOs) on nickel-based homogeneous catalysts .[1–3] The coordination-insertion mechanism, also known as the Cossee-Arlman mechanism, and the metallacycle mechanism have been proposed on these homogeneous nickel catalysts to describe oligomer chain growth on these materials. The Cossee-Arlman mechanism involves coordination and subsequent insertion of olefin molecules and has been postulated on nickel-based homogeneous catalysts for ethylene oligomerization through comparisons of external and internal oligomer selectivities from reinsertion and the inclusion of an alkylaluminium cocatalyst to form Ni-alkyl intermediates posited in the mechanism.[4–10] On the other hand, the metallacycle mechanism for ethylene oligomerization is associated with successive coordination of olefin molecules prior to carbon-carbon coupling and is proposed to produce LAOs, such as 1-butene and 1-hexene, on transition metal catalysts such as nickel, chromium, titanium, and tantalum in the absence of cocatalysts.[5,11,12]

Motivated by the high selectivity for LAOs in homogeneous nickel catalysts for olefin oligomerization, heterogeneous nickel-based catalysts have been formulated for this chemistry as they typically do not use cocatalysts or activators.[1,13] Prior work on heterogeneous nickel catalysts has supported the Cossee-Arlman mechanism for olefin oligomerization/dimerization based on comparisons of the Cossee-Arlman and metallacycle mechanisms from density functional theory (DFT) calculations,[14–22] infrared (IR) spectroscopy to illustrate kinetically relevant Ni-alkyl surface intermediates for olefin oligomerization,[21,23] analysis of isotopomer product distributions with ethylene and perdeuteroethylene mixtures,[18] use of nonconjugated diene probe molecules to evince coordination and insertion,[18] and hydrogen cofeeds to suggest a Ni-hydride intermediate.[24,25] Nevertheless, analysis of olefin oligomerization reactivity and mechanisms on heterogeneous nickel catalysts are often convoluted because typically only a fraction of nickel sites are active with[26,27] or without[20,28,29] the use of an activator, the catalyst deactivates on-stream,[19,23,30–33] and residual acid site reactivity induces competing pathways.[25,34,35]

While DFT, molecular cofeeds and probes, and spectroscopic methods can be used to elucidate the Cossee-Arlman mechanism for olefin oligomerization, analysis of the product selectivities at various process conditions is seldom performed to validate the mechanism. For ethylene oligomerization on nickel catalysts,

[a] Department of Chemical Engineering and Materials Science, University of Minnesota–Twin Cities, Minneapolis, Minnesota 55455, United States
[b] Department of Chemistry, Chemical Theory Center, and Supercomputing Institute, University of Minnesota–Twin Cities, Minneapolis, Minnesota 55455, United States
[c] Institute for Integrated Catalysis, Pacific Northwest National Laboratory, Richland, Washington 99352, United States
[d] Department of Chemistry and Catalysis Research Center, Technical University of Munich, 85748 Garching, Germany
[e] Department of Chemistry, The University of Chicago, Chicago, Illinois 60637, United States
Electronic Supplementary Information (ESI) available: [details of any supplementary information available should be included here]. See DOI: 10.1039/x0xx00000x

both sequential coordination-insertion and successive coordination of ethylene in the Cossee-Arlman and metallacycle mechanisms, respectively, yield butene product selectivities that are invariant with process conditions, as only one kinetic pathway occurs before the rate-limiting carbon-carbon coupling steps.[14–18] However, propylene can insert on nickel through either the α or β carbon in the Cossee-Arlman mechanism, which generates two distinct mechanistic pathways prior to the kinetically relevant step.[36–38] In contrast, successive coordination of propylene in the metallacycle mechanism invokes only one pathway prior to the kinetically relevant step. The distinct mechanistic pathways lead to pressure-dependent and pressure-independent hexene product selectivities that can be examined to differentiate the Cossee-Arlman and metallacycle mechanisms.

In our previous work, a nickel functionalized zirconium oxide-based metal organic framework (MOF) catalyst, Ni/UiO-66, was synthesized with isolated nickel atoms deposited on the zirconium oxide node through a missing linker defect, as evinced from comparisons between DFT-optimized cluster models and extended X-ray absorption fine structure (EXAFS) data.[19] This material was active for ethylene and 1-butene oligomerization devoid of cocatalysts.[19,20] Unprecedented stability for >10 days on-stream was observed during ethylene oligomerization, and only oligomers were detected to suggest absence of residual acid sites.[20] After undergoing an induction period and reaching steady state, butene formation rates increased after exposing the catalyst to higher ethylene pressures when comparing rates at the lower reference partial pressure.[20] This increase in rate was ascribed to an increase in nickel active site density, as higher ethylene pressures were proposed to facilitate a stoichiometric reaction to generate the catalytically relevant nickel-alkyl species during the induction period.[19,20] The nickel species for ethylene oligomerization were enumerated with in-situ NO titration experiments to normalize reaction rates, and steady state kinetics were measured to compare experimental and DFT-computed activation energies to validate the Cossee-Arlman mechanism.[20]

The unique stability for ethylene oligomerization on Ni/UiO-66, the ability to titrate active sites and normalize reaction rates, and the production of only oligomers proffers Ni/UiO-66 as a platform to study propylene oligomerization and the reaction mechanism. In the work presented herein, we report propylene oligomerization rates in the absence of a cocatalyst to measure steady state kinetics and hexene product selectivities. From steady state product selectivities, the Cossee-Arlman mechanism can be validated through analysis of the steady state rates and hexene product selectivities that are a function of pressure.

2. Experimental

2.1 Catalyst Synthesis and Characterization

An ideal UiO-66 material is a zirconium oxide (Zr_6O_8) based MOF connected with twelve terephthalate ligands.[39–43] Nickel can be functionalized on the Zr_6O_8 node through a missing linker defect to form Ni/UiO-66.[19,20,44–47] The detailed synthesis of UiO-66 and deposition of nickel onto the inorganic node to formulate Ni/UiO-66 is described elsewhere.[19,20,43] Powder X-ray diffraction (PXRD), N_2 isotherms, thermal gravimetric analysis (TGA), temperature programmed oxidation (TPO), proton nuclear magnetic resonance (^{1}H NMR) spectroscopy on the digested Ni/UiO-66 MOF, scanning transmission electron microscopy−energy dispersive X-ray spectroscopy (STEM-EDS), inductively coupled plasma−atomic emission spectroscopy (ICP-AES), IR spectroscopy, and X-ray adsorption spectroscopy (XAS) data for the as-synthesized Ni/UiO-66 were reported previously.[19,20] Briefly, the as-synthesized Ni/UiO-66 had a surface area of 1301 m^2 g^{-1} with ~0.7 nickel atoms per zirconium oxide node.[20]

2.2 Catalytic Testing

Ni/UiO-66 was pressed (<6.9 MPa), pelletized, and sieved to obtain particle sizes of 180-420 μm (40-80 mesh). The sample (10-80 mg) was physically mixed with sand (~200 mg, subjected prior to an overnight wash in 2 M HNO_3 solution followed by DI water rinse until pH ~7, and a final thermal treatment in flowing dry air (0.83 cm^3 s^{-1}) at 1273 K (0.083 K s^{-1} ramp rate from ambient temperature) for 16 h; $10 < wt_{diluent}/wt_{cat} < 15$) and then packed between two quartz wool plugs (Technical Glass Products) in a tubular glass-lined stainless-steel reactor (6.35 mm O.D. and 4 mm I.D., SGE Analytical Science). The free volume of the reactor was filled with quartz rods (3 mm O.D.; Technical Glass Products) to prevent vertical displacement of the catalyst bed. The temperature was measured using a K-type thermocouple (Omega) wrapped around the periphery of the stainless-steel reactor with the tip placed at the center of the catalyst bed and regulated with an electronic controller (Watlow), respectively. The catalyst was pretreated in helium (Matheson, 99.997%, 0.83 cm^3 s^{-1}) from ambient temperature to 573 K (0.08 K s^{-1}) for 4 hours and then cooled to reaction temperature (473 K) in flowing helium. Propylene (Matheson, 99.83%, 0.08-0.83 cm^3 s^{-1}) was introduced to the reactor with mass flow controllers (Brooks 5850E Series) and pressurized (105-550 kPa) using a back-pressure regulator (TESCOM Series 44-2300) placed downstream of the reactor with the gas-phase pressure measured using a pressure transducer (Omega) placed upstream of the reactor. Propylene gas phase pressures less than 105 kPa were obtained by feeding a mixture of helium (Matheson, 99.997%) and propylene at ambient pressure. The composition of the reactor effluent was quantified using a gas chromatograph (Agilent GC 7890A) equipped with a dimethylpolysiloxane HP-1 column (50 m × 320 μm × 0.52 μm) connected to a flame ionization detector (FID).

2.3 In-Situ NO Titrations

The reactor setup is identical to the one described above. A nitric oxide/nitrogen mixture (Airgas, 1% NO, balance N_2, 0.083-0.17 cm^3 s^{-1}) was introduced in the propylene gas stream at various pressures (500 – 550 kPa) with a mass flow controller (Brooks 5850E Series). An online mass spectrometer (MKS Cirrus 2) was utilized to determine the effluent propylene, hexene, NO, and N_2 signals (m/z: 42, 84, 30, and 28, respectively). The N_2 flow was used as a tracer to determine the average residence time of NO over the catalyst bed, which was normalized and used to calculate the amount of NO reacted/absorbed on nickel sites to suppress the rate of propylene oligomerization.

2.4 Cluster Models of Ni/UiO-66 and Kohn-Sham Density Functional Theory (DFT) Calculations

Cluster models of Ni/UiO-66 were derived from a truncated Zr_6 node of an optimized periodic structure of UiO-66 with formate groups capping the inorganic linker.[48] One formate group was removed and replaced with a $[Ni(OH)_2)]^{-1}$ group as nickel is deposited on the zirconium oxide node through missing linker defects,[16,17,45] to give the cluster model formula of $[NiZr_6(\mu_3\text{-}OH)_3(\mu_3\text{-}O)_5(OH)_2]^{11+} \bullet 11(CHO_2^{-1})$.[49] Kohn-Sham DFT calculations were performed with the M06-L density functional[50] implemented in the Gaussian 16 software package.[51] The def2-SVP and def2-TZVPP basis sets were used for C, H, and O atoms and Zr and Ni atoms, respectively,[52,53] and the SDD effective core potential was implemented for Zr atoms.[54] All cluster models and the individual gas phase olefin molecules were optimized, except the C atoms capping the Zr_6 node to maintain the framework structure and rigidity.[48] Zero-point energies and thermal contributions to enthalpies and Gibbs free energies were calculated from vibrational frequency calculations at 298.15 K and 101.3 kPa.

3. Results and Discussion

3.1 Catalyst Performance and Active Site Enumeration

Figure 1 presents propylene oligomerization rates normalized by the total amount of nickel in Ni/UiO-66 with time on stream at 473 K and 5 kPa, 106 kPa, 259 kPa, and 500 kPa devoid of cocatalysts. The induction periods on Ni/UiO-66 for propylene oligomerization at 106 kPa and 500 kPa are ~2 ks and ~8 ks which are significantly shorter than the induction periods of ~150 ks and ~85 ks, respectively, for ethylene oligomerization on the same material at the same partial pressures.[20] It is postulated that induction periods are controlled by a heterolytic C-H dissociation step to generate a [Ni-ethenyl]$^-$ species and [μ-OH]$^+$ complex for ethylene dimerization and are necessary to form the kinetically relevant Ni-alkyl species.[1,14,20,32,33] In our previous work, the induction period was attributed to the in-situ generation of relevant Ni-ethyl species during ethylene oligomerization, and higher ethylene pressures were required to create these active sites, as reference reaction rates increased after exposing the catalyst to higher ethylene pressures.[20] However, for propylene oligomerization, as shown in Figure S1, the catalyst returns to the same reaction rates at 5 kPa after exposing the catalyst to 500 kPa of propylene, suggesting that no additional active sites are formed at higher propylene pressures. The observed invariance in the induction period with propylene pressure shown in Figure 1 and in the number of Ni-alkyl species at different propylene pressures (Figure S1) plausibly arises because propylene has a weaker allylic C-H bond compared to the vinylic C-H bond of ethylene, where the former more readily forms the relevant Ni-alkyl species.[55] While there are slight variations in the length of induction period when changing propylene pressures from 5 – 500 kPa as shown in Figure 1, these changes are minor compared to the days-long transients observed with ethylene oligomerization at similar ethylene pressures as relevant Ni-alkyl species are much more more rapidly formed during propylene oligomerization. The catalyst appears to be stable for propylene oligomerization, with the reaction rate decreasing <5% over 150 minutes. The steady state rates that are reported hereafter are those that are examined with a reference condition and do not change within 10% (Figure S3).

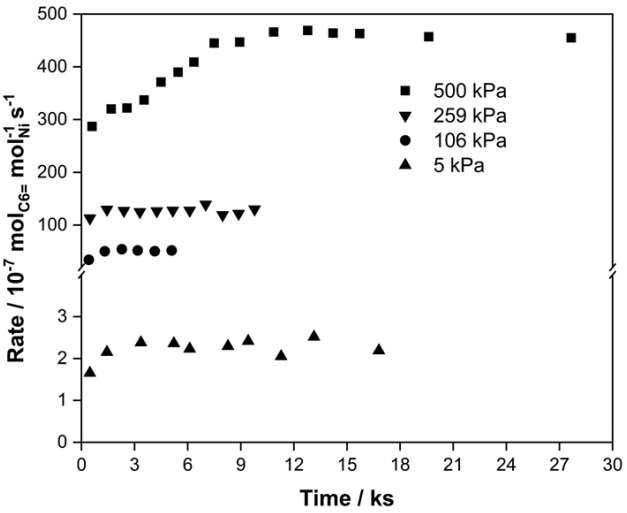

Figure 1 Propylene oligomerization rates as a function of time on stream on Ni/UiO-66 at 500 kPa (■), 259 kPa (▼), 106 kPa (●) and 5 kPa (▲) at 473 K.

Normalization of reaction rates is required to study reaction kinetics, as not all nickel species are active or yield the same reactivity during olefin oligomerization.[20,28,29] In a prior report, we noted that incorrect reaction orders are obtained when nickel active site densities are not enumerated because active site densities increase with increasing pressure. This results in enhancement in reaction rates from an increase in site densities and from higher ethylene pressures being conflated. In-situ NO titrations enable us to disambiguate these contributions because the number of Ni species relevant for catalysis could be precisely determined and reaction rates could be normalized by measured site densities to determine the reaction orders for ethylene oligomerization.[20] Following the same experimental protocols, the number of nickel active sites were assessed with in-situ NO titration experiments during propylene oligomerization as shown in Figure 2. Once the catalyst reached steady state at 493 K and 550 kPa, a mixture of 1% NO and 99% N_2 was introduced to the reactant gas stream. A decrease in the hexene flowrate is observed when N_2 appears to break through the catalyst bed. The NO flow has a delayed breakthrough response, suggesting that NO titrates the nickel active sites on Ni/UiO-66 to impede the rate of hexene formation. The number of nickel active sites can be enumerated by mathematical integration between the NO and normalized N_2 breakthrough curves.[56,57] The number of nickel active sites enumerated during propylene oligomerization on Ni/UiO-66 is ~20 μmol g_{cat}^{-1}, which is about 5% of nickel species from the ~430 μmol g_{cat}^{-1} of nickel in the MOF, as determined by ICP-AES, assuming one NO molecule binds to one nickel atom.[20] This value is consistent with prior work showing that not all Ni species are active for catalysis on Ni/UiO-66 MOFs during ethylene oligomerization.[20] Data from another in-situ NO titration experiment at 500 kPa and 473 K are presented in Figure S6 to affirm that ~5% of nickel sites are active for propylene oligomerization.

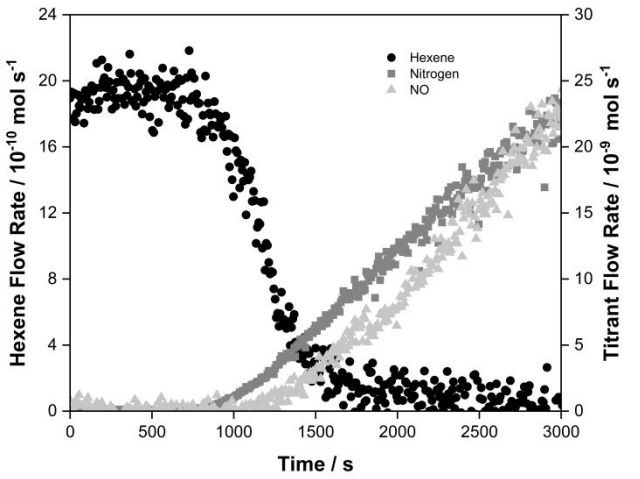

Figure 2 In situ NO titration showing a decrease in the rate of hexene formation (●) upon introduction of 0.083 cm^3 s^{-1} of 1% NO (▲, light grey) and 99% N_2 (■, dark gray) in 0.83 cm^3 s^{-1} at a total pressure of 550 kPa at 493 K on 90.8 mg of Ni/UiO-66

3.2. Mechanisms and Kinetics for Propylene Oligomerization

The Cossee-Arlman and metallacycle mechanisms are proposed on heterogeneous nickel-based catalysts for olefin oligomerization.[14,25] In Scheme 1, we present the Cossee-Arlman mechanism for propylene oligomerization, showing the formation of all possible hexene isomers with nickel proposed to remain in the 2+ oxidation state throughout the entire cycle.[21,38] This mechanism is often posited on the basis of the inclusion of alkylaluminum cocatalysts that form Ni-alkyl species.[18,27,38,47] However, observed induction periods in the absence of activators during olefin oligomerization are often attributed to the creation of relevant nickel-hydride or nickel-alkyl species during catalysis.[1,20,21,25,32,33,58] The mechanism is proposed to start with a nickel-hydride species (**A**) that binds to a propylene molecule (**B**). Species **B** can undergo two distinct regioselective hydride insertions to either form a 2,1-propyl species (**C**) or a 1,2-propyl species (**D**). Another propylene molecule can coordinate to **C** and **D** to yield species **E** and **F**, respectively. Regioselective 2,1 and 1,2 olefin insertions, which are proposed to be the kinetically relevant steps, proceed on species **E** and **F** to generate four distinct Ni-hexyl species.[14–19] The Ni-hexyl species undergo β-hydride elimination to generate a nickel hydride species and the resulting hexene product that desorbs to regenerate **A** and form 4-methylpentenes (**4MP**), 2,3-dimethylbutenes (**DMB**), linear hexenes (**LH**), and 2-methylpentenes (**2MP**).

The metallacycle mechanism for propylene oligomerization on Ni/UiO-66, shown in Scheme 2, is also proposed on heterogeneous catalysts.[5,14,25,31,59] This mechanism is postulated on catalysts for olefin oligomerization without the use of cocatalysts or observed induction periods due to the direct successive insertion of olefin molecules.[1] The active species for the metallacycle mechanism is proposed to be Ni^+ or Ni^{2+} ions (**G**) that undergo successive coordination of two propylene molecules, where the singly and doubly-coordinated propylene molecule on the nickel site are denoted as **H** and **I**, respectively.[1,14] Species **I** undergoes oxidative coupling, which is the slow step of the catalytic sequence, to form three distinct metallacyclopentane intermediates.[14,15] The metallacyclopentane intermediates undergo successive β-hydride and reductive elimination steps to regenerate **G** and produce **4MP**, **DMB**, **LH**, and **2MP**.

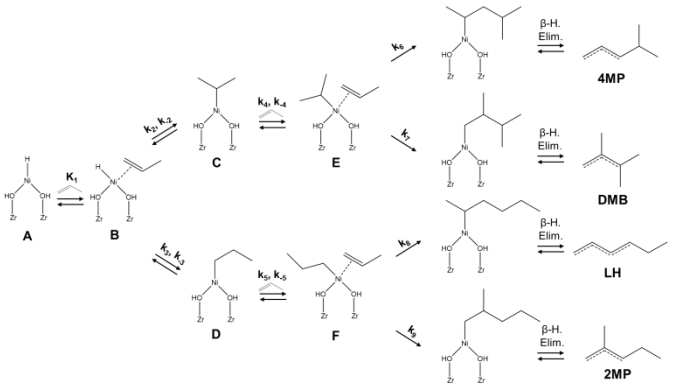

Scheme 1: Cossee-Arlman mechanism for propylene oligomerization on Ni/UiO-66. Note the entire node is omitted for clarity.

The Cossee-Arlman mechanism on Ni/UiO-66 is considered to propagate olefin oligomerization over the metallacycle mechanism for ethylene and butene oligomerization due to observed induction periods in the absence of cocatalysts, persistence of Ni species in the 2+ oxidation state before and after reaction as determined by X-ray adsorption near edge structure (XANES) analysis, and agreement of apparent activation energies between experiment and computation with DFT.[19,20] In Figure 1, short induction periods are observed to indicate in-situ generation of kinetically relevant Ni-alkyl species relevant for propylene oligomerization devoid of activators. Previous work has suggested that these induction periods are accompanied with in-situ generation of dienes,[14,20,21,33] which is consistent with the observed hexadiene formation in this study as shown in Figure S2. When comparing the XANES spectra for the Ni/UiO-66 after thermal treatment and at steady state during propylene oligomerization (Figure S7a), no change in the pre-edge region is observed. The peak at 8333 eV persists and is consistent with the presence of nickel(II) species assessed using a α-$Ni(OH)_2$ reference from our previous work[19] to suggest that nickel remains as 2+ during reaction, in line with the Cossee-Arlman mechanism.

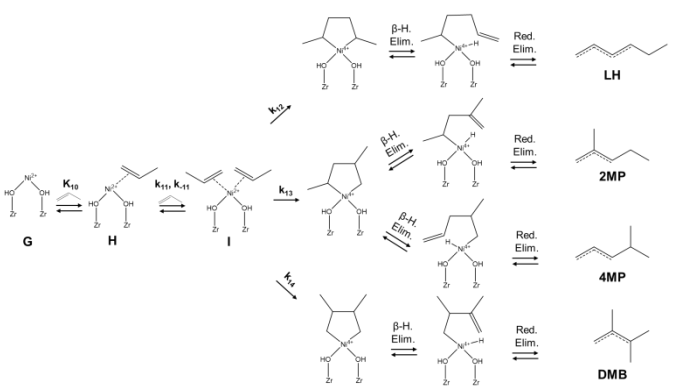

Scheme 2: Metallacycle mechanism for propylene oligomerization on Ni/UiO-66. Note the entire node is omitted for clarity.

Steady state reaction orders and comparisons among experimental and computed activation energies can be examined to validate the Cossee-Arlman mechanism on Ni/UiO-66 for olefin oligomerization after normalization of reaction rates by the number of relevant active sites.[19,20] The reaction was determined to be first order in propylene pressure from 5 kPa to 500 kPa at 473 K on Ni/UiO-66, as shown Figure 3a in line with observations of ethylene and 1-butene oligomerization being first order in olefin pressure on Ni/UiO-66.[19,20] Assuming only two propylene molecules are required to make hexene products, this suggests that a singly-coordinated propylene species on the nickel active site is the most abundant surface intermediate (MASI). From 453 K to 493 K, an Arrhenius plot in Figure 3b reveals an apparent activation energy of 21.0 ± 3.4 kJ mol^{-1}, 24.6 ± 3.8 kJ mol^{-1}, 15.7 ± 2.2 kJ mol^{-1}, and 17.5 ± 2.8 kJ mol^{-1} for **4MP**, **DMB**, **LH**, and **2MP**, respectively. These activation energies are lower than experimentally measured activation energies of 81 kJ mol^{-1} and 58 kJ mol^{-1} for ethylene and butene oligomerization on Ni/UiO-66 and lower than those measured on Ni-Na-X and Ni-MIL-127 for propylene oligomerization at 35 kJ mol^{-1} and ~60 kJ mol^{-1}, respectively.[19–21,30] From the computed Gibbs free energy diagrams of the Cossee-Arlman mechanism using DFT on cluster models of Ni/UiO-66 shown in Figures S8-S11, the olefin insertion steps have the highest barriers, ranging from 88 kJ mol^{-1} to 143 kJ mol^{-1} depending on the hexene product being formed, and thus, C-C bond formation is the kinetically relevant step. For **LH**, the intrinsic free energy barrier for the olefin insertion is 96 kJ mol^{-1} which is in good agreement with the olefin insertion barriers for ethylene and butene oligomerization for the formation of linear dimers on Ni/UiO-66 of 80 kJ mol^{-1} and 87 kJ mol^{-1}.[19,20] From the first order kinetics determined in Figure 3a that suggests the resting state of the catalyst is a Ni-propyl species, the calculated apparent activation barrier from the Ni-propyl MASI, **D**, and the olefin insertion step for **LH**, is 21 kJ mol^{-1}, as shown in Figure S10, which is in good agreement with the apparent activation energy of 15.7 kJ mol^{-1} obtained from experiment to corroborate the Cossee-Arlman mechanism. Energy diagrams for all other products and thermodynamic values for intermediates for the Cossee-Arlman mechanism are reported in Section S5.

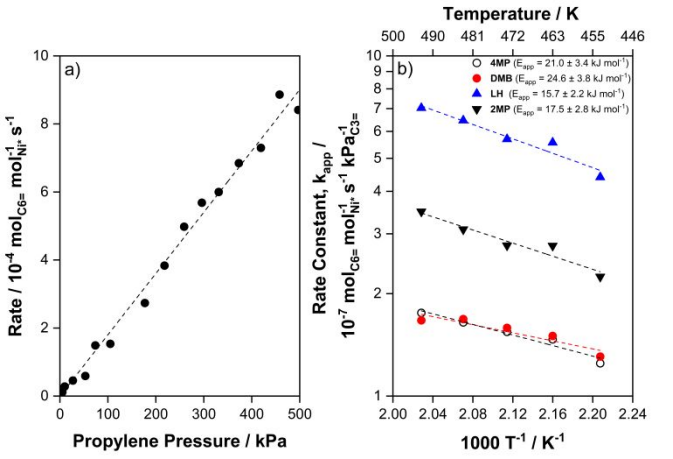

Figure 3 (a) Hexene formation rate versus propylene partial pressure (5–500 kPa) at 473 K and (b) Arrhenius plot at 259 kPa for propylene oligomerization from 453 K to 493 K for 4MP (○), DMB (●), LH(▲), and 2MP (▼) on Ni/UiO-66.

3.3. Hexene Product Selectivities for Propylene Oligomerization

While previous work on Ni/UiO-66 has presented evidence for the Cossee-Arlman mechanism for olefin oligomerization, we propose that the Cossee-Arlman and metallacycle mechanisms can be more broadly evinced through analysis of hexene product selectivities and product selectivity ratios derived from rate expressions for the proposed mechanisms. The rate expression and selectivity for species i is denoted as r_i and s_i, respectively, with rate constants and equilibrium constants for each elementary step denoted as k_j and K_j, respectively, from Schemes 1 and 2 for the Cossee-Arlman and metallacycle mechanisms, respectively. From DFT calculations, the kinetically relevant step for the Cossee-Arlman mechanism is the olefin insertion step on heterogeneous nickel catalysts.[14–19] In our system, the proposed rate expressions for **4MP**, **DMB**, **LH**, and **2MP** assuming the olefin insertion step is kinetically limiting for the Cossee-Arlman mechanism are shown in Equations 1-4 respectively, based on Scheme 1.

$$r_{\mathbf{4MP}} = k_6[\mathrm{E}] \quad (1)$$

$$r_{\mathbf{DMB}} = k_7[E] \quad (2)$$

$$r_{\mathbf{LH}} = k_8[F] \quad (3)$$

$$r_{\mathbf{2MP}} = k_9[F] \quad (4)$$

Assuming the first adsorption step between **A** and **B** is quasi-equilibrated and all surface-bound species before the kinetically relevant step are at pseudo-steady state, the rate expressions for **4MP**, **DMB**, **LH**, and **2MP** can be derived to only be expressed in terms of propylene pressures and the density of unoccupied nickel sites **A**, as shown in Equations 5-8 (See Section S4 for derivation).

$$r_{\mathbf{4MP}} = \frac{k_6 k_4 k_2 K_1 [A] P_{C_3H_6}^2}{(k_{-4} + k_6 + k_7)\left(k_{-2} - \frac{k_{-4} k_4 P_{C_3H_6}}{k_{-4} + k_6 + k_7} + k_4 P_{C_3H_6}\right)} \quad (5)$$

$$r_{\mathbf{DMB}} = \frac{k_7 k_4 k_2 K_1 [A] P_{C_3H_6}^2}{(k_{-4} + k_6 + k_7)\left(k_{-2} - \frac{k_{-4} k_4 P_{C_3H_6}}{k_{-4} + k_6 + k_7} + k_4 P_{C_3H_6}\right)} \quad (6)$$

$$r_{\mathbf{LH}} = \frac{k_8 k_5 k_3 K_1 [A] P_{C_3H_6}^2}{(k_{-5} + k_8 + k_9)\left(k_{-3} - \frac{k_{-5} k_5 P_{C_3H_6}}{k_{-5} + k_8 + k_9} + k_5 P_{C_3H_6}\right)} \quad (7)$$

$$r_{\mathbf{2MP}} = \frac{k_9 k_5 k_3 K_1 [A] P_{C_3H_6}^2}{(k_{-5} + k_8 + k_9)\left(k_{-3} - \frac{k_{-5} k_5 P_{C_3H_6}}{k_{-5} + k_8 + k_9} + k_5 P_{C_3H_6}\right)} \quad (8)$$

The selectivity for **4MP**, **DMB**, **LH**, and **2MP** for the Cossee-Arlman mechanism can be derived from Equations 5-8 (see Section S4 for derivation) and these expressions are shown in Equations 9-12 with α, β, γ, δ, and ε defined in Equation 13-17. The selectivity for all hexene isomers is a function of propylene pressure as shown in Equations 9-12.

$$s_{\mathbf{4MP}} = \frac{\frac{k_6}{k_6 + k_7}(\beta + \delta P_{C_3H_6})}{\varepsilon(\alpha + \gamma P_{C_3H_6}) + (\beta + \delta P_{C_3H_6})} \quad (9)$$

$$s_{\mathbf{DMB}} = \frac{\frac{k_7}{k_6 + k_7}(\beta + \delta P_{C_3H_6})}{\varepsilon(\alpha + \gamma P_{C_3H_6}) + (\beta + \delta P_{C_3H_6})} \quad (10)$$

$$s_{\mathbf{LH}} = \frac{\frac{k_8}{k_8 + k_9}(\alpha + \gamma P_{C_3H_6})}{(\alpha + \gamma P_{C_3H_6}) + \frac{1}{\varepsilon}(\beta + \delta P_{C_3H_6})} \quad (11)$$

$$s_{\mathbf{2MP}} = \frac{\frac{k_9}{k_8 + k_9}(\alpha + \gamma P_{C_3H_6})}{(\alpha + \gamma P_{C_3H_6}) + \frac{1}{\varepsilon}(\beta + \delta P_{C_3H_6})} \quad (12)$$

$$\alpha = k_{-2} \quad (13)$$

$$\beta = k_{-3} \quad (14)$$

$$\gamma = k_4 - \frac{k_{-4} k_4}{k_{-4} + k_6 + k_7} \quad (15)$$

$$\delta = k_5 - \frac{k_{-5} k_5}{k_{-5} + k_8 + k_9} \quad (16)$$

$$\varepsilon = \frac{(k_8 + k_9) k_5 k_3 (k_{-4} + k_6 + k_7)}{(k_6 + k_7) k_4 k_2 (k_{-5} + k_8 + k_9)} \quad (17)$$

Based on the Cossee-Arlman mechanism (Scheme 1), products **4MP** and **DMB** are both formed from **C**, while products **LH** and **2MP** are both formed from **D**. Consequently, the ratio between **4MP** and **DMB** and the ratio between **LH** and **2MP** should only be a function of the olefin insertion rate constants, as shown in Equations 18 and 19. This ratio arises simply from the possibility of propylene undergoing a 2,1- or 1,2- insertion for both intermediates **E** and **F**, which can be clearly seen from Equations 1-4. The two branching mechanistic pathways prior to the kinetically relevant step can be evaluated from the products derived from **C**, **4MP** + **DMB**, and **D**, **LH** + **2MP**, as shown in Equation 20, which shows that the selectivity ratio of **LH** + **2MP** to **4MP** + **DMB** is pressure dependent due to adsorption of a propylene molecule to form **E** and **F** from **C** and **D**, respectively. Thus, Equations 9-12 and 18-20 can be used to assess the coordination of propylene and insertion characteristics that would result from the Cossee-Arlman mechanism, which suggest that product selectivities and selectivity ratios are a function of propylene pressure.

$$S_{\frac{\mathbf{4MP}}{\mathbf{DMB}}} = \frac{k_6}{k_7} \quad (18)$$

$$S_{\frac{\mathbf{LH}}{\mathbf{2MP}}} = \frac{k_8}{k_9} \quad (19)$$

$$S_{\frac{\mathbf{LH+2MP}}{\mathbf{4MP+DMB}}} = \frac{(\alpha + \gamma \boldsymbol{P_{C_3H_6}})}{(\beta + \delta \boldsymbol{P_{C_3H_6}})} * \varepsilon \quad (20)$$

Selectivity characteristics of hexene isomers are distinct when considering the metallacycle mechanism and can be determined by deriving rate expressions for the mechanism shown in Scheme 2. The oxidative coupling step has been proposed to be the kinetically relevant step for olefin oligomerization via the metallacycle mechanism based on previous DFT calculations.[14,15,19] The proposed rate expressions from **4MP**, **DMB**, **LH**, and **2MP** following the metallacycle mechanism (See Section S4) are shown in Equations 21-24. Assuming the first adsorption from **G** to **H** is quasi-equilibrated and the formation of species **I** is at pseudo-steady state, the rate expressions can be derived and only expressed in terms of propylene pressure and unoccupied nickel sites **G**.

$$r_{\mathbf{4MP}} = k_{13}[I] = \frac{k_{13} k_{11} K_{10} [\mathrm{G}] P_{C_3H_6}^2}{k_{-11} + k_{12} + k_{13} + k_{14}} \quad (21)$$

$$r_{\mathbf{DMB}} = k_{14}[I] = \frac{k_{14} k_{11} K_{10} [\mathrm{G}] P_{C_3H_6}^2}{k_{-11} + k_{12} + k_{13} + k_{14}} \quad (22)$$

$$r_{\mathbf{LH}} = k_{12}[I] = \frac{k_{12} k_{11} K_{10} [\mathrm{G}] P_{C_3H_6}^2}{k_{-11} + k_{12} + k_{13} + k_{14}} \quad (23)$$

$$r_{\mathbf{2MP}} = k_{13}[I] = \frac{k_{13} k_{11} K_{10} [\mathrm{G}] P_{C_3H_6}^2}{k_{-11} + k_{12} + k_{13} + k_{14}} \quad (24)$$

From the rate expressions shown in Equations 21-24, product selectivities for **4MP**, **DMB**, **LH**, and **2MP** can be derived as shown in Equations 25-28 for the metallacycle mechanism. Additionally, the ratio of product selectivities are only a ratio of rate constants and are not pressure dependent (Equation 29).

Uniquely, the ratio of product selectivities for **2MP** and **4MP** is proposed to be unity in the metallacycle mechanism (Equations 21 and 24), as these two products share the same oxidative coupling step, and the distinct isomers are formed from the β-hydride elimination step after the kinetically relevant step. Thus, individual product selectivities (Equations 25-28) and the ratio of product selectivities (Equation 29) are pressure-independent for the metallacycle mechanism.

$$S_{\mathbf{4MP}} = \frac{k_{13}}{k_{12} + 2k_{13} + k_{14}} \quad (25)$$

$$S_{\mathbf{DMB}} = \frac{k_{14}}{k_{12} + 2k_{13} + k_{14}} \quad (26)$$

$$S_{\mathbf{LH}} = \frac{k_{12}}{k_{12} + 2k_{13} + k_{14}} \quad (27)$$

$$S_{\mathbf{2MP}} = \frac{k_{13}}{k_{12} + 2k_{13} + k_{14}} \quad (28)$$

$$S_{\frac{(LH+2MP)}{(4MP+DMB)}} = \frac{k_{12} + k_{13}}{k_{13} + k_{14}} \quad (29)$$

From the selectivity expressions and ratios derived from the Cossee-Arlman (Equations 9-12 and 18-20) and metallacycle mechanisms (Equations 25-29), the former and latter are pressure-dependent and pressure-independent respectively. These differences in product selectivities being pressure-dependent or pressure-independent arise from the inherent mechanistic pathways, where the metallacycle mechanism is characteristic of successive coordination before the kinetically relevant olefin coupling while the Cossee-Arlman mechanism coordinates and inserts an olefin molecule before coordinating and inserting a second olefin molecule. Thus, only one pathway occurs before the kinetically relevant step in the metallacycle mechanism, while two pathways arise via a 2,1- or 1,2- hydride insertion step to form **C** and **D** in the Cossee-Arlman mechanism.

In Figure 4, individual product selectivities for **4MP**, **DMB**, **LH**, and **2MP** are shown as a function of propylene pressure from 5-220 kPa to evaluate the verisimilitude of the Cossee-Arlman or metallacycle mechanism for propylene oligomerization on Ni/UiO-66. At low propylene pressures (<50 kPa), the selectivities of **LH** and **2MP** increase with increasing propylene pressure while the selectivities of **4MP** and **DMB** decrease with increasing propylene pressure until all product selectivities become invariant with propylene pressure (> 50 kPa). These selectivity characteristics are consistent with selectivity expressions derived in Equation 9-12 for the Cossee-Arlman mechanism where all product selectivities are a function of propylene pressure. Furthermore, the selectivities of **4MP** and **DMB** decrease together while the selectivities of **LH** and **2MP** increase together, which is consistent with the products of **4MP** and **DMB** forming from intermediate **C** and with products **LH** and **2MP** forming from intermediate **D**, where **C** and **D** are two distinct Ni-propyl intermediates posited in the Cossee-Arlman mechanism.[38]

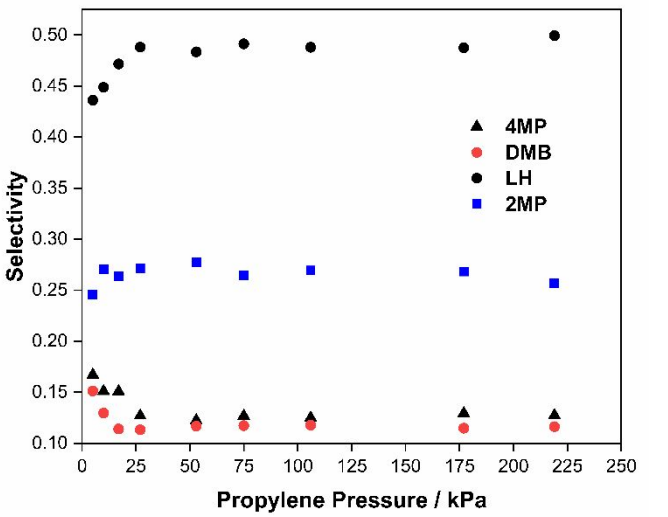

Figure 4 Selectivity of **4MP** (▲), **DMB** (●), **LH** (●), and **2MP** (■) as a function of propylene pressure at 473 K on Ni/UiO-66.

In Figure 5a, ratios of **4MP** to **DMB** (Equation 18), of **LH** to **2MP** (Equation 19), and of **2MP** to **4MP** (Equations 21 and 24) are plotted as a function of propylene pressure at 473 K from 5 to 220 kPa to further assess the plausibility of the Cossee-Arlman or metallacycle mechanism on Ni/UiO-66. Comparing the ratio of selectivities of **4MP** to **DMB** (blue) and of **LH** to **2MP** (black) as shown in Figure 5a, the two distinct product ratios are unaffected by propylene pressure, which are consistent with Equation 18 and Equation 19, respectively, for the Cossee-Arlman mechanism. However, when comparing the selectivity ratio of **2MP** to **4MP**, the ratio increases as a function of pressure at low propylene pressures (<50 kPa) and approaches a value of ~2. The latter observation is incongruous with the metallacycle mechanism as the expected ratio should be pressure independent and be a value of unity (Equations 21 and 24). In Figure 4b, the ratio of **LH** + **2MP** to **4MP** + **DMB** is plotted against propylene partial pressure from 5 kPa to 220 kPa at 473 K. At low propylene pressures (<50 kPa), the ratio of **LH** + **2MP** to **4MP** + **DMB** is function of propylene pressure before it becomes invariant with propylene pressure, consistent with the selectivity expression derived in Equation 20 from the Cossee-Arlman mechanism. The individual product selectivities and ratios of selectivities from Figures 4 and 5 are all consistent with Equations 9-12 and 18-20, respectively, to suggest propylene oligomerization occurs via the Cossee-Arlman mechanism on Ni/UiO-66. The Cossee-Arlman and metallacycle mechanisms can be distinguished based on sequential coordination and insertion branching pathways, which give unique product selectivities as a function of propylene pressure.

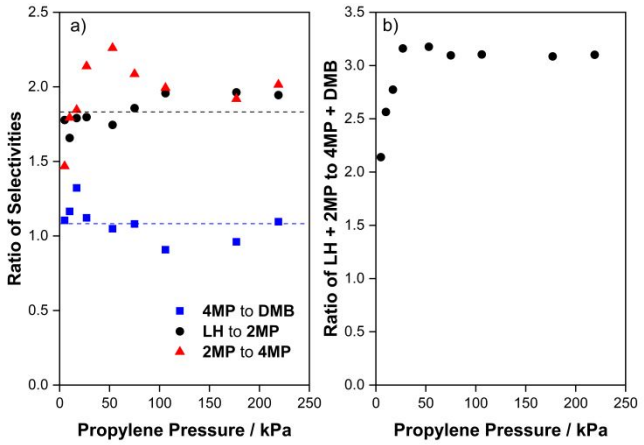

Figure 5 Ratio of selectivities for (a) **4MP** to **DMB** (■), **LH** to **2MP** (●), **2MP** to **4MP** (▲), where the dashed lines are meant to guide the eye and (b) **LH** + **2MP** to **4MP** + **DMB** at 473 K on Ni/UiO-66

4. Conclusion

This work affirms propagation of the Cossee-Arlman mechanism over the metallacycle mechanism on Ni/UiO-66 for olefin oligomerization, specifically for propylene oligomerization, through observations of induction periods in the absence of cocatalysts, analysis of the nickel(II) oxidation state through XANES, and comparison of apparent activation energies through experiment and DFT. This study also illustrates a new method to discriminate between the Cossee-Arlman and metallacycle mechanisms based on hexene product selectivities derived from rate expressions for each mechanism. The former shows that the product selectivities and selectivity ratios are a function of olefin pressure, consistent with observations reported herein to confirm the Cossee-Arlman mechanism.

Conflicts of interest

There are no conflicts to declare.

Acknowledgements

This work was supported by the Inorganometallic Catalyst Design Center and the Catalyst Design for Decarbonization Center, Energy Frontier Research Centers funded by the U.S. Department of Energy (DOE), Office of Science, Basic Energy Sciences (BES), under Awards DE-SC0012702 and DE-SC0023383. B.Y. acknowledges the National Science Foundation for a graduate research fellowship and a departmental fellowship funded by 3M. The authors acknowledge the Minnesota Supercomputing Institute (MSI) at the University of Minnesota for providing computational resources for this research. Part of this work was performed at the Stanford Synchrotron Radiation Lightsource (SSRL) of SLAC National Accelerator Laboratory by Co-ACCESS, supported by the US Department of Energy, Office of Basic Energy Sciences, Chemical Sciences, Geosciences, and Biosciences Division with the help from Dr. Adam Hoffman, Dr. Jiyun Hong, and Dr. Simon Bare. We thank Krishna Iyer and Ting Lin for helpful technical discussions.

References

1 R. Joshi, A. Saxena and R. Gounder, *Catal. Sci. Technol.*, 2020, **10**, 7101–7123.
2 A. Forestière, H. Olivier-Bourbigou and L. Saussine, *Oil Gas Sci. Technol.*, 2009, **64**, 649–667.
3 H. Olivier-Bourbigou, P. A. R. Breuil, L. Magna, T. Michel, M. F. Espada Pastor and D. Delcroix, *Chem. Rev.*, 2020, **120**, 7919–7983.
4 J. Skupińska, *Chem. Rev.*, 1991, **91**, 613–648.
5 F. Speiser, P. Braunstein and L. Saussine, *Acc. Chem. Res.*, 2005, **38**, 784–793.
6 W. Keim, *Angew. Ch*, 1990, **29**, 235–244.
7 W. Keim, *Angew. Chemie - Int. Ed.*, 2013, **52**, 12492–12496.
8 S. D. Ittel, L. K. Johnson and M. Brookhart, *Chem. Rev.*, 2000, **100**, 1169–1203.
9 C. M. Killian, L. K. Johnson and M. Brookhart, *Organometallics*, 1997, **16**, 2005–2007.
10 M. A. Escobar, O. S. Trofymchuk, B. E. Rodriguez, C. Lopez-Lira, R. Tapia, C. Daniliuc, H. Berke, F. M. Nachtigall, L. S. Santos and R. S. Rojas, *ACS Catal.*, 2015, **5**, 7338–7342.
11 H. Grubbs and A. Miyashita, *J.C.S. Chem. Comm.*, 1977, **63**, 864–865.
12 H. Grubbs and A. Miyashita, *J. Am. Chem. Soc.*, 1978, **100**, 7416–7418.
13 A. Finiels, F. Fajula and V. Hulea, *Catal. Sci. Technol.*, 2014, **4**, 2412–2426.
14 R. Y. Brogaard and U. Olsbye, *ACS Catal.*, 2016, **6**, 1205–1214.
15 V. Bernales, A. B. League, Z. Li, N. M. Schweitzer, A. W. Peters, R. K. Carlson, J. T. Hupp, C. J. Cramer, O. K. Farha and L. Gagliardi, *J. Phys. Chem. C*, 2016, **120**, 23576–23583.
16 J. Ye, L. Gagliardi, C. J. Cramer and D. G. Truhlar, *J. Catal.*, 2017, **354**, 278–286.
17 J. Ye, L. Gagliardi, C. J. Cramer and D. G. Truhlar, *J. Catal.*, 2018, **360**, 160–167.
18 E. D. Metzger, R. J. Comito, C. H. Hendon and M. Dincă, *J. Am. Chem. Soc.*, 2017, **139**, 757–762.
19 J. Zheng, L. Löbbert, S. Chheda, N. Khetrapal, J. Schmid, C. Alberto Gaggioli, B. Yeh, R. Bermejo-Deval, R. Kishan Motkuri, M. Balasubramanian, J. L. Fulton, O. Y. Gutiérrez, J. Ilja Siepmann, M. Neurock, L. Gagliardi and J. A. Lercher, *J. Catal.*, 2022, **413**, 176–183.
20 B. Yeh, S. P. Vicchio, S. Chheda, J. Zheng, J. Schmid, L. Löbbert, R. Bermejo-Deval, O. Y. Gutiérrez, J. A. Lercher, C. C. Lu, M. Neurock, R. B. Getman, L. Gagliardi and A. Bhan, *J. Am. Chem. Soc.*, 2021, **143**, 20274–20280.
21 B. Yeh, S. Chheda, S. D. Prinslow, A. S. Hoffman, J. Hong, J. E. Perez-Aguilar, S. R. Bare, C. C. Lu, L. Gagliardi and A. Bhan, *J. Am. Chem. Soc.*, 2023, **145**, 3408–3418.

22 L. Löbbert, S. Chheda, J. Zheng, N. Khetrapal, J. Schmid, R. Zhao, C. A. Gaggioli, D. M. Camaioni, R. Bermejo-Deval, O. Y. Gutiérrez, Y. Liu, J. I. Siepmann, M. Neurock, L. Gagliardi and J. A. Lercher, *J. Am. Chem. Soc.*, 2023, **145**, 1407–1422.

23 A. Ehrmaier, Y. Liu, S. Peitz, A. Jentys, Y. H. C. Chin, M. Sanchez-Sanchez, R. Bermejo-Deval and J. Lercher, *ACS Catal.*, 2019, **9**, 315–324.

24 S. Moussa, P. Concepción, M. A. Arribas and A. Martínez, *ACS Catal.*, 2018, **8**, 3903–3912.

25 R. Joshi, G. Zhang, J. T. Miller and R. Gounder, *ACS Catal.*, 2018, **8**, 11407–11422.

26 H. Chevreau, A. Permyakova, F. Nouar, P. Fabry, C. Livage, F. Ragon, A. Garcia-Marquez, T. Devic, N. Steunou, C. Serre and P. Horcajada, *CrystEngComm*, 2016, **18**, 4094–4101.

27 E. D. Metzger, C. K. Brozek, R. J. Comito and M. Dinca, *ACS Cent. Sci.*, 2016, **2**, 148–153.

28 I. Agirrezabal-Telleria and E. Iglesia, *J. Catal.*, 2017, **352**, 505–514.

29 A. N. Mlinar, S. Shylesh, O. C. Ho and A. T. Bell, *ACS Catal.*, 2014, **4**, 337–343.

30 A. N. Mlinar, G. B. Baur, G. G. Bong, A. Getsoian and A. T. Bell, *J. Catal.*, 2012, **296**, 156–164.

31 M. Lallemand, A. Finiels, F. Fajula and V. Hulea, *J. Phys. Chem. C*, 2009, **113**, 20360–20364.

32 R. Henry, M. Komurca, Y. Ganjkhanlou, R. Y. Brogaard, L. Lu, K.-J. Jens, G. Berlier and U. Olsbye, *Catal. Today*, 2018, **299**, 154–163.

33 R. Y. Brogaard, M. Kømurcu, M. M. Dyballa, A. Botan, V. Van Speybroeck, U. Olsbye and K. De Wispelaere, *ACS Catal.*, 2019, **9**, 5645–5650.

34 V. Hulea and F. Fajula, *J. Catal.*, 2004, **225**, 213–222.

35 M. Lallemand, O. A. Rusu, E. Dumitriu, A. Finiels, F. Fajula and V. Hulea, *Appl. Catal. A Gen.*, 2008, **338**, 37–43.

36 Z. Xu, D. Zhao, J. P. Chada, D. C. Rosenfeld, J. L. Rogers, I. Hermans and G. W. Huber, *J. Catal.*, 2017, **354**, 213–222.

37 A. Jonathan, N. M. Eagan, D. L. Bruns, S. S. Stahl, M. P. Lanci, J. A. Dumesic and G. W. Huber, *Catal. Sci. Technol.*, 2021, **11**, 3599–3608.

38 R. J. Comito, E. D. Metzger, Z. Wu, G. Zhang, C. H. Hendon, J. T. Miller and M. Dincă, *Organometallics*, 2017, **36**, 1681–1683.

39 J. H. Cavka, S. Jakobsen, U. Olsbye, N. Guillou, C. Lamberti, S. Bordiga and K. P. Lillerud, *J. Am. Chem. Soc.*, 2008, **130**, 13850–13851.

40 G. C. Shearer, S. Chavan, S. Bordiga, S. Svelle, U. Olsbye and K. P. Lillerud, *Chem. Mater.*, 2016, **28**, 3749–3761.

41 S. Biswas and P. Van Der Voort, *Eur. J. Inorg. Chem.*, 2013, 2154–2160.

42 C. A. Trickett, K. J. Gagnon, S. Lee, F. Gándara, H. B. Bürgi and O. M. Yaghi, *Angew. Chemie - Int. Ed.*, 2015, **54**, 11162–11167.

43 M. J. Katz, Z. J. Brown, Y. J. Colón, P. W. Siu, K. A. Scheidt, R. Q. Snurr, J. T. Hupp and O. K. Farha, *Chem. Commun.*, 2013, **49**, 9449–9451.

44 H. G. T. Nguyen, N. M. Schweitzer, C. Y. Chang, T. L. Drake, M. C. So, P. C. Stair, O. K. Farha, J. T. Hupp and S. T. Nguyen, *ACS Catal.*, 2014, **4**, 2496–2500.

45 A. M. Abdel-Mageed, B. Rungtaweevoranit, M. Parlinska-Wojtan, X. Pei, O. M. Yaghi and R. Jürgen Behm, *J. Am. Chem. Soc.*, 2019, **141**, 5201–5210.

46 T. A. Goetjen, X. Zhang, J. Liu, J. T. Hupp and O. K. Farha, *ACS Sustain. Chem. Eng.*, 2019, **7**, 2553–2557.

47 J. Liu, J. Ye, Z. Li, K. I. Otake, Y. Liao, A. W. Peters, H. Noh, D. G. Truhlar, L. Gagliardi, C. J. Cramer, O. K. Farha and J. T. Hupp, *J. Am. Chem. Soc.*, 2018, **140**, 11174–11178.

48 V. Bernales, M. A. Ortuño, D. G. Truhlar, C. J. Cramer and L. Gagliardi, *ACS Cent. Sci.*, 2018, **4**, 5–19.

49 N. Planas, J. E. Mondloch, S. Tussupbayev, J. Borycz, L. Gagliardi, J. T. Hupp, O. K. Farha and C. J. Cramer, *J. Phys. Chem. Lett.*, 2014, **5**, 3716–3723.

50 Y. Zhao and D. G. Truhlar, *J. Chem. Phys.*, 2006, **125**, 1–18.

51 M. J. Frisch, G. W. Rucks, H. B. Schlegel, G. E. Scuseria, G. Robb, M. A. Cheeseman, J. R. Scalmani, V. Barone, G. A. Petersson, H. Nakatsuji, X. Li, M. Caricato, A. V. Marenich, J. Bloino, B. G. Janesko, R. Gomperts, B. Mennucci, H. P. Hratchian, J. V. Ortiz, A. F. Izmaylov, J. L. Sonnenberg, D. Williams-Young, F. Ding, F.; Lipparini, J. Egidi, F.; Goings, A. Peng, B.; Petrone, T. Henderson, D. Ranasinghe, V. G. Zakrzewski, J. Gao, N. Rega, G. Zheng, W. Liang, M. Hada, M. Ehara, K. Toyota, R. Fukuda, J. Hasegawa, M. Ishida, T. Nakajima, Y. Honda, O. Kitao, H. Nakai, T. Reven, K. Throssell, J. Montgomery, J. A., J. E. Peralta, F. Ogliaro, M. J. Bearpark, J. J. Heyd, E. N. Brothers, K. N. Kudin, V. N. Staroverov, T. A. Keith, R. Kobayashi, J. Normand, K. Raghavachari, A. P. Rendell, J. C. Burant, S. S. Iyengar, J. Tomasi, M. Cossi, J. M. Millam, M. Klene, C. Adamo, R. Cammi, J. W. Ochterski, R. L. Martin, K. Morokuma, O. Farkas, J. B. Foresman and D. J. Fox, 2016.

52 F. Weigend and R. Ahlrichs, *Phys. Chem. Chem. Phys.*, 2005, **7**, 3297–3305.

53 F. Weigend, *Phys. Chem. Chem. Phys.*, 2006, **8**, 1057–1065.

54 D. Andrae, U. Häußermann, M. Dolg, H. Stoll and H. Preuß, *Theor. Chim. Acta*, 1990, **77**, 123–141.

55 Edward P. Hunter and Sharon G. Lias, in *NIST Chemistry WebBook, NIST Standard Reference Database Number 69*, eds. P.J. Linstrom and W.G. Mallard, National Institute of Standards and Technology, Gaithersburg MD, 20899.

56 S. Afrin and P. Bollini, *J. Catal.*, 2022, **413**, 76–80.

57 W. S. Lee, A. Kumar, Z. Wang and A. Bhan, *ACS Catal.*, 2015, **5**, 4104–4114.

58 I. Agirrezabal-Telleria and E. Iglesia, *J. Catal.*, 2020, **389**, 690–705.

59 R. D. Andrei, M. I. Popa, F. Fajula, C. Cammarano, A. Al Khudhair, K. Bouchmella, P. H. Mutin and V. Hulea, *ACS Catal.*, 2015, **5**, 2774–2777.